ACS APPLIED ENERGY MATERIALS

Letter

Photoacoustic imaging of lithium metal batteries

Huihui Liu, Yibo Zhao, Jiasheng Zhou, Ping Li, Shou-Hang Bo, and Sung-Liang Chen

ACS Appl. Energy Mater., **Just Accepted Manuscript** • DOI: 10.1021/acsaem.9b01791 • Publication Date (Web): 05 Nov 2019

Photoacoustic imaging of lithium metal batteries

Huihui Liu,[1,‡] Yibo Zhao,[1,‡] Jiasheng Zhou,[1] Ping Li,[1] Shou-Hang Bo,[*,1] and Sung-Liang Chen[*,1,2]

[1]University of Michigan-Shanghai Jiao Tong University Joint Institute, Shanghai Jiao Tong University, Shanghai 200240, China

[2]State Key Laboratory of Advanced Optical Communication Systems and Networks, Shanghai Jiao Tong University, Shanghai 200240, China

*E-mails: shouhang.bo@sjtu.edu.cn (S.H.Bo); sungliang.chen@sjtu.edu.cn (S.L.Chen)

‡These authors contribute equally to this work.

ABSTRACT. To better understand and overcome the lithium (Li) dendrite problem in Li metal batteries, great efforts have been made to reveal dendrite growth processes using various imaging modalities. However, because of being almost invisible to electrons and X-rays, directly imaging Li metal with the required contrast, spatial and temporal resolutions have always been the challenge. Here, we show that by exploiting photoacoustic effect, microscale-resolution three-dimensional structure of Li protrusions inside the glass fiber separator of a Li/Li liquid electrolyte symmetric cell can be clearly visualized with high contrast within minutes by photoacoustic microscopy, demonstrating the potential for observing dendrite growth.

KEYWORDS. Battery imaging, lithium batteries, dendrites, photoacoustic imaging, photoacoustic microscopy, three-dimensional imaging.

TEXT.

Lithium (Li)-ion batteries are ubiquitous in present-day technological applications, ranging from portable devices, electric vehicles to grid-scale stationary energy storage. Li-ion batteries are composed of positive and negative electrodes (two Li reservoirs with different concentrations) which are separated by a polymeric membrane, i.e., a separator. The separator is immersed in Li-ion conducting liquid electrolyte which permits only Li-ion shuffling between the positive and negative electrodes during battery cycling. Simultaneously, electrons flow through the external circuit powering electronic devices.

With increasing demand for higher-energy batteries, it is now a common consensus that graphite anode in Li-ion batteries must be replaced with the most energy-dense Li metal in the next-generation Li metal batteries.[1] Ironically, Li metal anode was the choice when the first rechargeable Li battery was invented in the 1970th.[2] Soon afterwards, however, safety hazards associated with Li metal anode were identified, which halted the development of Li metal batteries. The problem is inhomogeneous deposition (during charge) and stripping (during discharge) of Li metal, which forms protrusions into the separator (commonly referred to as dendrites in literature) instead of smooth deposits, leading to short circuit and even explosion of Li metal batteries.[3] The microstructure of such Li metal protrusions can be mossy, whisker-like

or dendritic, and is a complex function of cycling duration, rate, temperature, and electrolyte concentration, to name a few. Solid-state batteries utilizing a mechanically strong and non-flammable solid-state electrolyte have been proposed as a promising solution to suppress dendrite growth of Li metal. However, recent studies have shown that metal dendrites can still grow through the grain boundaries of a solid electrolyte and eventually lead to electrolyte crack and short circuit of the battery.[4] It is therefore of uttermost importance to develop a quantitative understanding of Li metal dendrite growth in conventional liquid electrolyte and current solid-state electrolyte settings, and to identify conditions under which smooth Li deposition of tens of micrometers in thickness can be achieved.

Imaging technologies have been demonstrated as a powerful tool to study dendrite growth.[4–17] For example, scanning and transmission electron microscopy has been widely used to acquire images of Li dendrites with high resolution and high quality.[4,9,11–14] While electron microscopy shows the potential to provide the insight into the formation of dendrites, demanding sample preparation is required. Therefore, it is highly challenging for observation *in situ*, which is essential to track the dynamic evolution of Li metal dendrites during the charge and discharge cycles. Three-dimensional (3D) images of subsurface structures underneath Li metal dendrites were observed with X-ray tomography with resolution on the order of a micrometer.[6] However, more than a thousand images were collected with a series of data processing steps required, which restricts the temporal resolution of this technique, limiting its use to *ex situ* observations only. We further note that Li metal is neither visible to electrons nor to X-rays because Li possesses the third lowest electron density of all chemical elements (just above hydrogen and helium), making the observation of bulk Li metal through electron and X-ray microscopy impossible. Only the surfaces of Li metal which are composed of decomposition products

resulting from the side reaction between Li metal and the electrolyte (e.g., LiF and Li_2CO_3) can be visualized. Neutron depth profiling and neutron radiography have been shown to be important tools to probe spatial distribution of Li metal, track inactive Li and study Li dendrite growth in operando during cycling, providing fundamental insights into the plating and striping behavior of Li metal.[16,17] Nevertheless, neutron sources and spatial resolution of neutron imaging are both limited. Magnetic resonance imaging (MRI) was utilized to non-invasively observe and quantify Li metal microstructures.[5,8,10,15] However, Li is inherently insensitive to MRI (e.g., much less than that of proton),[10] limiting both the spatial and temporal resolution of ^{6}Li and ^{7}Li MRI.[5] Optical microscopy (OM) offers one possible route to *in situ* imaging of dendrites with high temporal resolutions, yet only two-dimensional (2D) images can be obtained.[9] Finally, because of limited penetration depth, most of these techniques discussed above cannot directly visualize Li dendrite growth within the separator or solid-state electrolyte membrane, an important area to precisely locate the positions and patterns of short circuits caused by metal protrusions.

Photoacoustic imaging is based on the photoacoustic effect that light absorbed by a material can be converted into heat and the subsequent thermoelastic expansion to generate an acoustic wave. In the past 20 years, it has been extensively explored in the biomedical imaging field to reveal a wide variety of endogenous or exogenous absorbers.[18–29] Since light is highly absorbed by most metals, we anticipate that Li metal can be visualized and quantified by photoacoustic imaging. In this paper, for the first time, we demonstrate that photoacoustic imaging can be exploited to map Li protrusions in Li metal batteries in 3D. A home-built photoacoustic microscopy (PAM) system is used to successfully observe the microstructure of Li protrusions inside the separator of a Li/Li liquid electrolyte symmetric cell. Although we image Li metal to demonstrate the utility of photoacoustic imaging, the obtained results suggest that photoacoustic imaging can potentially

be a new tool to realize, real-time imaging of Li as well as other metals, such as sodium and magnesium.[22,25] We believe that PAM can also be extended to image Li metal dendrite growth in solid-state batteries. The imaging technique is also cost-effective and easy to operate.

The details of the Li/Li cell sample fabrication, packaging, and charging can be found in Supporting Information. PAM imaging system used in this work was also described in Supporting Information. The lateral and axial resolutions of our PAM system were 3.3 μm (Figure S2c) and 26 μm (Figure S2d), respectively. The damage threshold of the Li/Li cell was calibrated to be >86 nJ, and the penetration depth in the cell by PAM was estimated, which are elaborated in Supporting Information.

Several imaging experiments were demonstrated to show the PAM's ability in studying Li protrusions. Firstly, Co-registered PAM and OM imaging of the Li-deposited electrode, the side with Li deposition after charging the Li/Li cell, was conducted for comparison of the two imaging modalities. The Li/Li cell sample was prepared, which was charged under current density of 0.5 mA/cm^2 for 15 hours. To facilitate image co-registration of PAM and OM, some makers were made on the top surface of a sample holder (Figure 1a) by using an ink pen. Li was deposited along the +Y direction upon electrochemical charging (Figure S1d). Figure 1 shows PAM maximum amplitude projection (MAP) (XY) and OM images of the Li/Li cell sample. The markers can be clearly seen in Figures 1b and 1c. Note that Figures 1c and 1e were taken by 5× and 20× objectives, respectively. As can be seen, by comparing co-registered PAM and OM images in Figures 1b and 1c, PAM enables much higher contrast. Besides, by comparing co-registered PAM and OM images in Figures 1d and 1e, PAM provides larger depth of focus (DOF). Further, Figure 1f shows the 3D rendering image of Figure 1d, demonstrating the 3D

imaging capability of PAM. By contrast, OM suffers from low contrast, limited DOF, and no depth information.

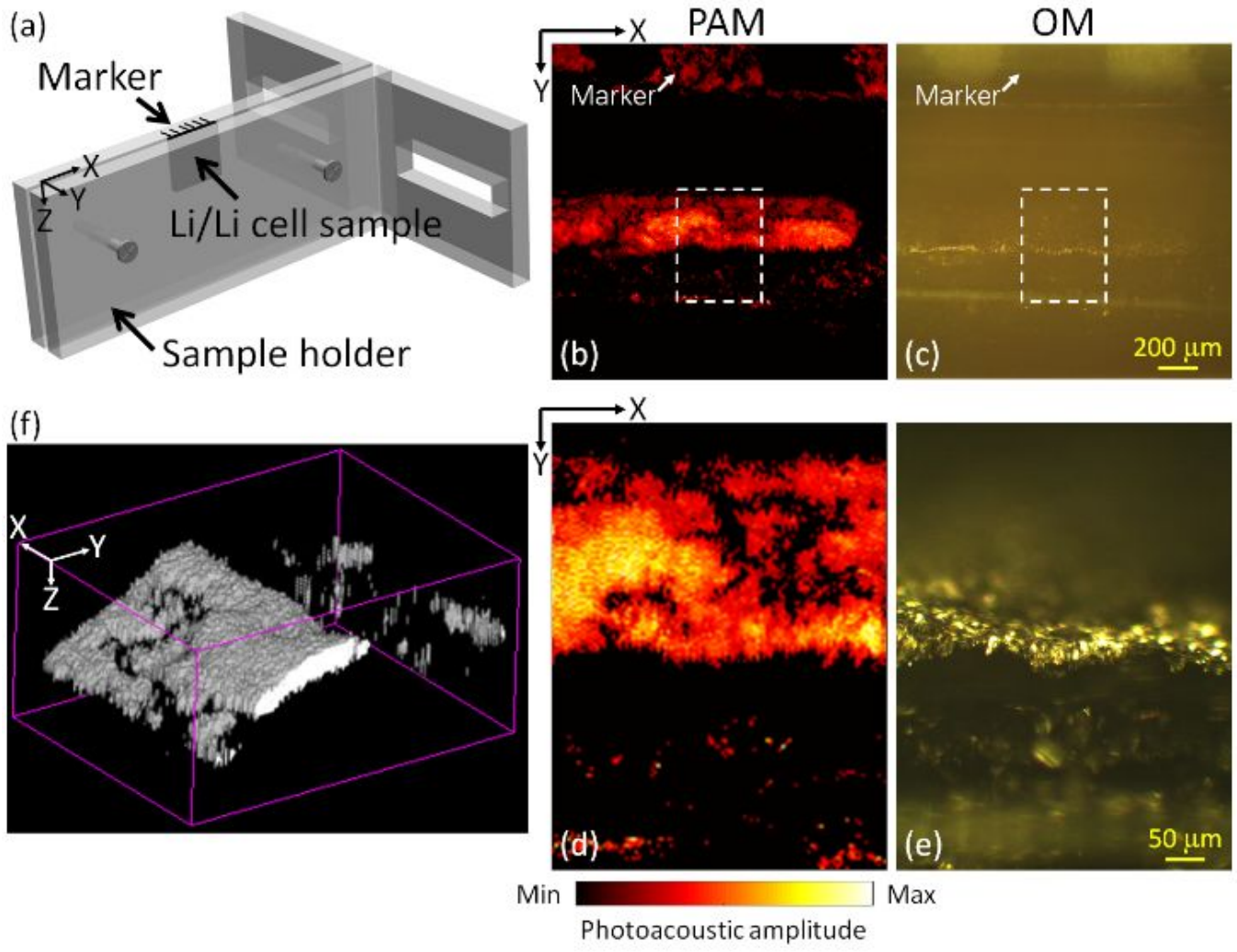

Figure 1. Comparison of PAM and OM for imaging Li of the Li/Li cell. (a) Schematic of the Li/Li cell sample and markers. (b) PAM MAP (XY) image of the Li/Li cell sample. (c) OM image of the Li/Li cell sample taken by using a 5× objective. (d) Zoom image of the dashed box in (b). (e) OM image of the Li/Li cell sample taken by using a 20× objective, corresponding to the dashed box region in (c). (b) and (c) are co-registered PAM and OM images, and so do (d) and (e). (b) and (c) share the same scale bar in (c), and (d) and (e) share the same scale bar in (e). (f) 3D rendering image of (d). 3D video of (f) is available (Movie 1). The XYZ orientation is the same as Figures S1 and S2.

Next, to demonstrate the imaging capability of PAM in visualization of Li protrusions from the Li-deposited electrode towards the glass fiber separator (GFS) of the Li/Li cell, the cross-sectional sidewall surface of one Li/Li cell sample before and after charging at current density of 1 mA/cm^2 for 15 hours was imaged. Figure 2 shows the PAM MAP (XY) images at two representative regions around the Li-deposited electrode of the Li/Li cell sample. As can be seen, before charging, a thin layer of the Li metal electrode with relatively uniform thickness was observed. By contrast, after charging, protrusions of Li metal from the Li-deposited electrode towards the GFS can be clearly identified. The fusion image shows the PAM image after charging overlaid with that before charging, providing a better comparison. The results suggest that Li protrusions after charging can be revealed by PAM. As can be observed in Figure 2, the thickness of the thin layer of the Li electrode before and after charging kept almost the same, which is considered to be plausible. Besides, Li protrusions were concentrated in certain areas of the Li-deposited electrode, demonstrating the inhomogeneous nature of Li deposition. The above-mentioned characteristics were observed in both of the two representative regions in Figure 2.

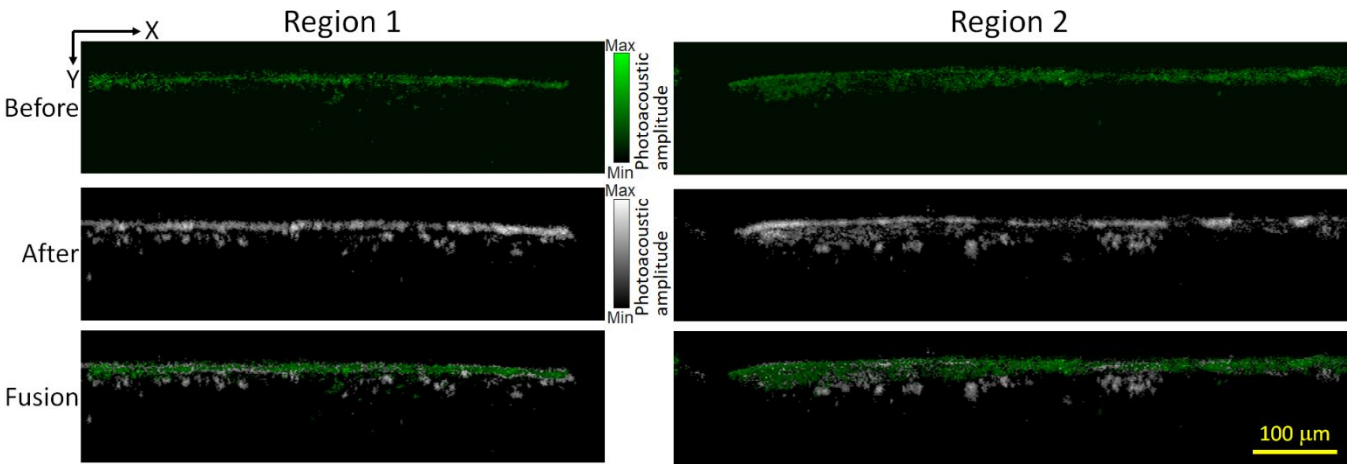

Figure 2. PAM MAP (XY) images at two representative regions around the Li metal electrode of the Li/Li cell sample before and after charging at current density of 1 mA/cm^2 for 15 hours. All images share the same scale bar. The XYZ orientation is the same as Figures S1 and S2.

Furthermore, because PAM is able to image Li protrusions, as demonstrated above, we attempted to utilize PAM to study quantitative changes of Li protrusions of the Li/Li cells under different charging current densities. Six Li/Li cell samples were prepared as follows: before charging and after charging under current densities of 0.1, 0.2, 0.3, 0.5, and 1 mA/cm^2, respectively, for 15 hours. Figure 3a shows the PAM MAP (XY) images of the six Li/Li cell samples. As can be seen, Li protrusions grew more and more as the charging current density increases. The Li thickness increased from ~0.11 mm for the case of before charging to ~0.54 mm for that of after charging at current density of 1 mA/cm^2. Figure 3b shows a representative 3D rendering image corresponding to the region labeled by the dashed box in the image of 1 mA/cm^2 in Figure 3a, demonstrating PAM's ability of 3D examination of Li protrusions inside the GFS. To quantify the Li protrusions under different current densities, the Li ratio, defined as the proportion of the area with Li over the observed area in 2D MAP images, was calculated. The calculation method of the Li ratio and error range is described in Supporting Information. As shown in Figure 3c, Li ratio increases gradually as increased charging current densities and reaches saturation at current density of 0.5 mA/cm^2. For charging current densities <0.5 mA/cm^2, the trend agrees with increasing amount of Li deposition as current density (or areal capacity) increases. However, in Figure 3c, the Li ratio for the case of 0.1 mA/cm^2 is lower than that for the case "Before," which is not reasonable. Another abnormal result is that above 0.5 mA/cm^2, no substantial increase of the Li ratio was observed as the current density doubled (i.e., from 0.5 mA/cm^2 to 1 mA/cm^2). This may be explained by the two limitations (finite imaging thickness and challenging sample preparation) discussed below, which compromise the accuracy of the quantified results to some degree.

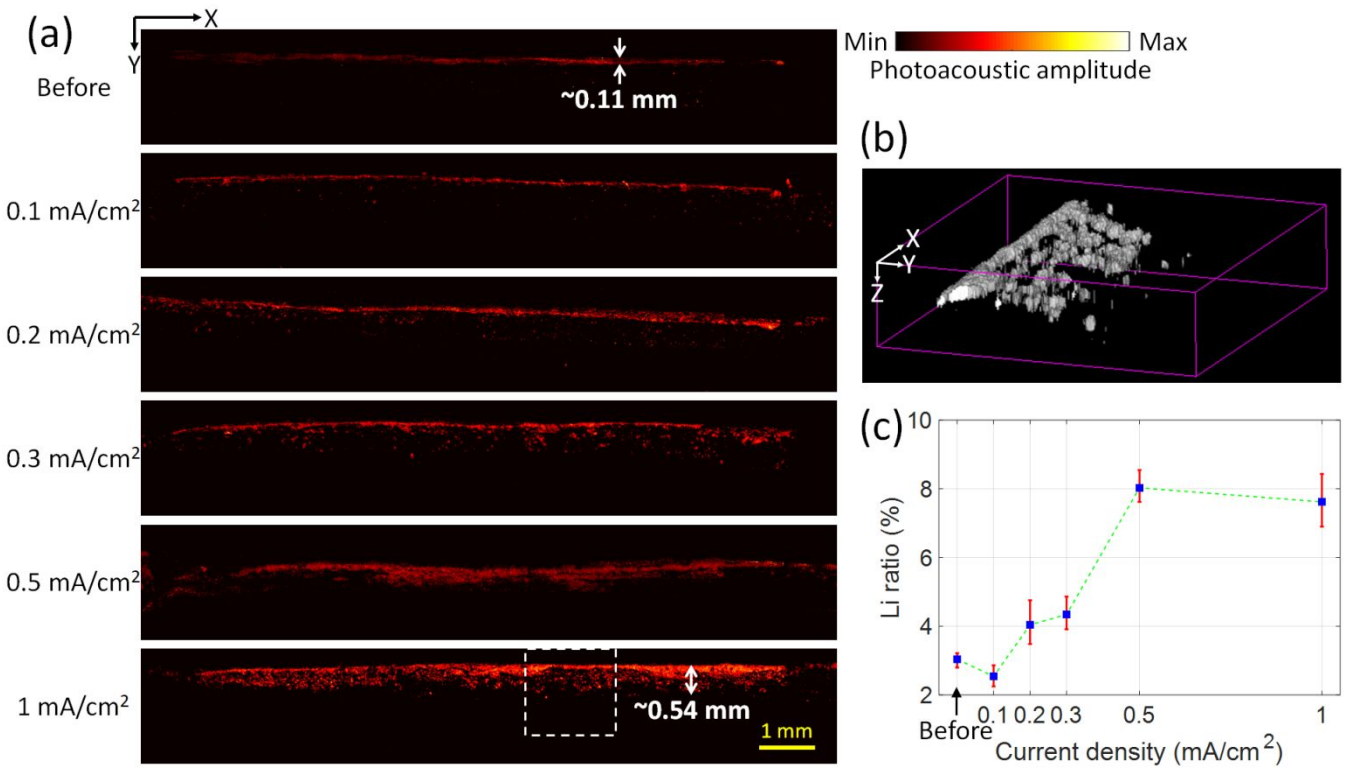

Figure 3. (a) PAM MAP (XY) images at regions around the Li metal electrode of the six Li/Li cell sample before and after charging at current densities of 0.1, 0.2, 0.3, 0.5, and 1 mA/cm^2, respectively, for 15 hours. All images share the same scale bar. (b) 3D rendering image corresponding to the region labeled by the dashed box in the image of 1 mA/cm^2 in (a). 3D video of (b) is available (Movie 2). (c) Quantitative changes of Li ratio. The XYZ orientation is the same as Figures S1 and S2.

Two limitations of PAM for this quantitative study are noticed (i.e., finite imaging thickness and challenging sample preparation), and possible solutions are discussed. (i) With the current light illumination along the Z direction in PAM (Figure 1a), only the top surface of Li protrusions (i.e., facing the –Z direction) can be visualized due to strong absorption of Li metal. To better quantify volumetric distribution of Li protrusions by PAM, dual-view PAM is a potential solution.[28] Furthermore, even with 160-µm penetration depth into the GFS, it is still impossible to image all Li metal contained in the GFS because the typical diameter of a GFS is on the order of centimeters and above. Development of a PAM sectioning tomography system could be

considered, which is similar to the idea of micro-optical sectioning tomography to obtain a high-resolution image of a whole mouse brain.[30] (ii) Six different pristine Li/Li cell samples were used in this study. The sample difference impaired the accuracy of the quantified Li protrusions. To improve the accuracy of quantification, the same Li/Li cell sample should be imaged by PAM before and after charging (the two images denoted as PAMb and PAMa, respectively). By subtracting PAMb from PAMa, more accurate quantification of Li protrusions can be obtained. However, we note the primary challenge associated with sample preparation. To ensure the quality of PAM imaging, a plastic bag with good light penetration was used in our study, yet this compromises the air tightness of the cell to some extent, which results in poor charge/discharge characteristics of the same Li/Li cell sample. In later studies, packaging materials of the cell that allow light penetration without air leakage must be identified.

In summary, PAM was exploited to image Li metal batteries to show potential of PAM as a novel tool to study mechanisms of Li metal dendrite growth. A PAM system with high spatial resolutions was used. Compared with OM, PAM was able to penetrate deeper down to ~160 μm inside the GFS. Further, PAM provided high contrast, large DOF, and depth information for imaging of Li in the Li/Li cell. Note that although OM can also penetrate inside the GFS with depth of ~50 μm (Figure S4), the contrast is much worse than PAM (e.g., Figure S4f for OM vs. Figure S4c for PAM). This manifests the qualitative improvement of PAM over OM in visualization of Li protrusions. The 3D rendering image of the Li/Li cell sample acquired by PAM was also demonstrated. Imaging result of one Li/Li cell sample before and after charging demonstrated the PAM ability in observation of Li protrusions. This proof-of-concept study shows that PAM offers a solution to the challenges suffered by existing technologies, such as the prohibitively high cost and demanding sample preparation in electron microscopy. There are

several advantages and potentials of PAM for imaging Li metal batteries: high resolution (in micrometers), 3D imaging capability, deep penetration into the separator, and high contrast from bulk Li metal. Currently, using our PAM system, the image acquisition time for an image consisting of 256 × 256 pixels was ~5 mins. As the aim of this study was to demonstrate the feasibility of this novel PAM approach for imaging Li metal batteries, the imaging speed was not optimized. According to recent studies,[22,25] high-speed and even real-time imaging can be realized by using a laser with a high pulse repetition rate and using either a MEMS-mirror scanner or a hexagon-mirror scanner in PAM. Besides, PAM imaging of batteries composed of other metal electrodes such as sodium, magnesium, and zinc would be technically possible and can be explored in future. Development of PAM imaging of Li metal batteries *in situ* would be of great interest for future work.

ASSOCIATED CONTENT

Supporting Information.

The following files are available free of charge.

Sample preparation of the Li/Li cell, PAM imaging system, calibrations of damage threshold and penetration depth, and calculation method of the Li ratio and error range (PDF)

AUTHOR INFORMATION

Corresponding Author

*E-mails: shouhang.bo@sjtu.edu.cn (S.H.Bo); sungliang.chen@sjtu.edu.cn (S.L.Chen)

Author Contributions

The manuscript was written through contributions of all authors. All authors have given approval to the final version of the manuscript. ‡H. Liu and Y. Zhao contributed equally.

Funding Sources

National Science Foundation of China (NSFC) (61775134) and Shanghai Sailing Program (18YF1411100).

Notes

The authors declare no competing financial interest.

ACKNOWLEDGMENT

We acknowledge financial support from the National Science Foundation of China (NSFC) and the Shanghai Sailing Program.

REFERENCES

(1) Liu, J.; Bao, Z.; Cui, Y.; Dufek, E.J.; Goodenough, J. B.; Khalifah, P.; Li, Q.; Liaw, B. Y.; Liu, P.; Manthiram, A.; Meng, Y. S.; Subramanian, V. R.; Toney, M. F.; Viswanathan, V. V.; Whittingham, M. S.; Xiao, J.; Xu, W.; Yang, J.; Yang, X.-Q.; Zhang, J.-G. Pathways for Practical High-Energy Long-cycling Lithium Metal Batteries. *Nat. Energy*. **2019**, *4*, 180-186.

(2) Whittingham, M. S. Electrical Energy Storage and Intercalation Chemistry. *Science*. **1976**, *192*, 1126-1127.

(3) Manthiram, A.; Yu, X.; Wang, S. Lithium Battery Chemistries Enabled by Solid-State Electrolytes. *Nat. Rev. Mater*. **2017**, *2*, 16103.

(4) Ren, Y.; Shen, Y.; Lin, Y.; Nan, C.-W. Direct Observation of Lithium Dendrites Inside Garnet-Type Lithium-Ion Solid Electrolyte. *Electrochem. Commun.* **2015**, *57*, 27-30.

(5) Chandrashekar, S.; Trease, N. M.; Chang, H. J.; Du, L. S.; Grey, C. P.; Jerschow, A. 7Li MRI of Li Batteries Reveals Location of Microstructural Lithium. *Nat. Mater.* **2012**, *11*, 311-315.

(6) Harry, K. J.; Hallinan, D. T.; Parkinson, D. Y.; MacDowell, A. A.; Balsara, N. P. Detection of Subsurface Structures Underneath Dendrites Formed on Cycled Lithium Metal Electrodes. *Nat. Mater.* **2014**, *13*, 69-73.

(7) Hou, H.; Cheng, L.; Richardson, T.; Chen, G.; Doeff, M.; Zheng, R.; Russo, R.; Zorba, V. Three-Dimensional Elemental Imaging of Li-Ion Solid-State Electrolytes Using Fs-Laser Induced Breakdown Spectroscopy (LIBS). *J. Anal. At. Spectrom*. **2015**, *30*, 2295-2302.

(8) Romanenko, K.; Jin, L.; Howlett, P.; Forsyth, M. In Situ MRI of Operating Solid-State Lithium Metal Cells Based on Ionic Plastic Crystal Electrolytes. *Chem. Mater.* **2016**, *28*, 2844-2851.

(9) Bai, P.; Li, J.; Brushett, F. R.; Bazant, M. Z. Transition of Lithium Growth Mechanisms in Liquid Electrolytes. *Energy Environ. Sci*. **2016**, *9*, 3221-3229.

(10) Ilott, A. J.; Mohammadi, M.; Chang, H. J.; Grey, C. P.; Jerschow, A. Real-Time 3D Imaging of Microstructure Growth in Battery Cells Using Indirect MRI. *Proc. Natl. Acad.*

Sci. U. S. A. **2016**, *113*, 10779-10784.

(11) Wang, C.; Gong, Y.; Dai, J.; Zhang, L.; Xie, H.; Pastel, G.; Liu, B.; Wachsman, E.; Wang, H.; Hu, L. In Situ Neutron Depth Profiling of Lithium Metal-Garnet Interfaces for Solid State Batteries. *J. Am. Chem. Soc.* **2017**, *139*, 14257-14264.

(12) Li, Y.; Li, Y.; Pei, A.; Yan, K.; Sun, Y.; Wu, C. L.; Joubert, L. M.; Chin, R.; Koh, A. L.; Yu, Y.; Perrino, J.; Butz, B.; Chu, S.; Cui, Y. Atomic Structure of Sensitive Battery Materials and Interfaces Revealed by Cryo-Electron Microscopy. *Science*. **2017**, *358*, 506-510.

(13) Wang, X.; Zhang, M.; Alvarado, J.; Wang, S.; Sina, M.; Lu, B.; Bouwer, J.; Xu, W.; Xiao, J.; Zhang, J. G.; Liu, J.; Meng, Y. S. New Insights on The Structure of Electrochemically Deposited Lithium Metal and Its Solid Electrolyte Interphases via Cryogenic TEM. *Nano Lett.* **2017**, *17*, 7606-7612.

(14) Zachman, M. J.; Tu, Z.; Choudhury, S.; Archer, L. A.; Kourkoutis, L. F. Cryo-STEM Mapping of Solid-Liquid Interfaces and Dendrites in Lithium-Metal Batteries. *Nature*. **2018**, *560*, 345-349.

(15) Chien, P. H.; Feng, X.; Tang, M.; Rosenberg, J. T.; O'Neill, S.; Zheng, J.; Grant, S. C.; Hu, Y. Y. Li Distribution Heterogeneity in Solid Electrolyte $Li_{10}GeP_2S_{12}$ upon Electrochemical Cycling Probed by ^{7}Li MRI. *J. Phys. Chem. Lett.* **2018**, *9*, 1990-1998.

(16) Lv, S.; Verhallen, T.; Vasileiadis, A.; Ooms, F.; Xu, Y.; Li, Z.; Li, Z.; Wagemaker, M. Operando monitoring the lithium spatial distribution of lithium metal anodes. *Nat. Commun.* **2018**, *9*, 2152.

(17) Song, B.; Dhiman, I.; Carothers, J. C.; Veith, G. M.; Liu, J.; Bilheux, H. Z.; Huq, A. Dynamic lithium distribution upon dendrite growth and shorting revealed by operando neutron imaging. *ACS Energy Lett.* **2019**, *4*, 2402-2408.

(18) Wang, L. V. Multiscale Photoacoustic Microscopy and Computed Tomography. *Nat. Photonics*. **2009**, *3*, 503-509.

(19) Wang, L. V.; Hu, S. Photoacoustic Tomography: In Vivo Imaging from Organelles to Organs. *Science*. **2012**, *335*, 1458-1462.

(20) Wang, L.; Maslov, L.; Wang, L. V. Single-Cell Label-Free Photoacoustic Flowoxigraphy in Vivo. *Proc. Natl. Acad. Sci. U. S. A*. **2013**, *110*, 5759-5764.

(21) Taruttis, A.; Ntziachristos, V. Advances in Real-Time Multispectral Optoacoustic Imaging and Its Applications. *Nat. Photonics*. **2015**, *9*, 219-227.

(22) Kim, J. Y.; Lee, C.; Park, K.; Lim, G.; Kim, C. Fast Optical-Resolution Photoacoustic Microscopy Using A 2-Axis Water-Proofing MEMS Scanner. *Sci. Rep*. **2015**, *5*, 7932.

(23) Hu, S. Listening to The Brain with Photoacoustics. *IEEE J. Sel. Top. Quantum Electron.* **2016**, *22*, 6800610.

(24) Li, L.; Zhu, L.; Ma, C.; Lin, L.; Yao, J.; Wang, L.; Maslov, K.; Zhang, R.; Chen, W.; Shi, J.; Wang, L. V. Single-Impulse Panoramic Photoacoustic Computed Tomography of Small-Animal Whole-Body Dynamics at High Spatiotemporal Resolution. *Nat. Biomed. Eng*. **2017**, *1*, 0071.

(25) Lan, B.; Liu, W.; Wang, Y. C.; Shi, J.; Li, Y.; Xu, S.; Sheng H.; Zhou, Q.; Zou, J.;

Hoffmann, U.; Yang, W.; Yao, J. High-Speed Widefield Photoacoustic Microscopy of Small-Animal Hemodynamics. *Biomed. Opt. Express.* **2018**, *9*, 4689-4701.

(26) Li, M.; Tang, Y.; Yao, J.; Photoacoustic Tomography of Blood Oxygenation: A Mini Review. *Photoacoustics*. **2018**, *10*, 65-73.

(27) Guo, Z.; Li, G.; Chen, S.-L. Miniature Probe for All-Optical Double Gradient-Index Lenses Photoacoustic Microscopy. *J. Biophotonics*. **2018**, *11*, e201800147.

(28) Cai, D.; Wong, T. T. W.; Zhu, L.; Shi, J.; Chen, S. L.; Wang, L. V. Dual-view photoacoustic microscopy for quantitative cell nuclear imaging. *Opt. Lett.* **2018**, *43*, 4875-4878.

(29) Guo, Z.; Li, Z.; Deng, Y.; Chen, S.-L. Photoacoustic Microscopy for Evaluating a Lipopolysaccharide-Induced Inflammation Model in Mice. *J. Biophotonics.* **2019**, *12*, e201800251.

(30) Li, A.; Gong, H.; Zhang, B.; Wang, Q.; Yan, C.; Wu, J.; Liu, Q.; Zeng, S.; Luo, Q. Micro-optical sectioning tomography to obtain a high-resolution atlas of the mouse brain. *Science.* **2010**, *330*, 1404-1408.

Table of Contents (TOC) graphic.

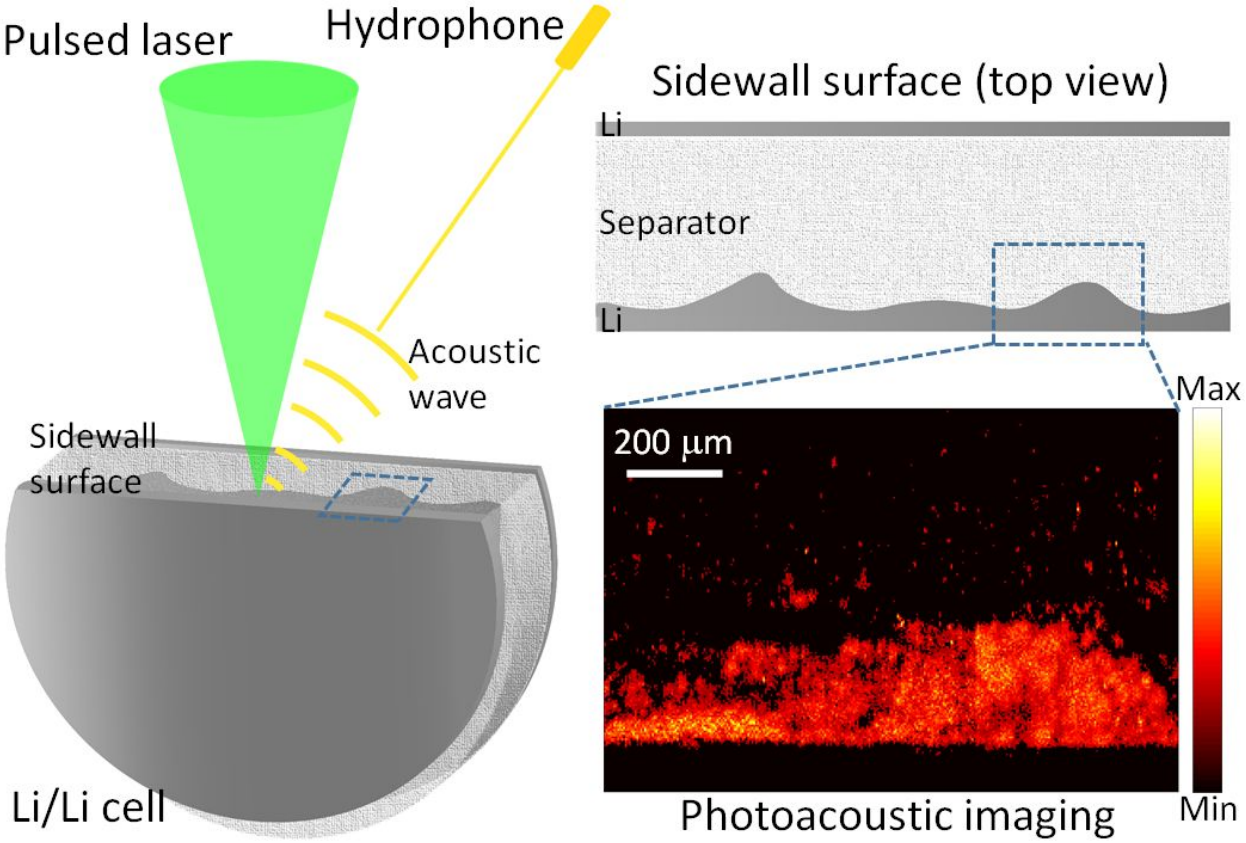
Pulsed laser
Hydrophone
Acoustic wave
Sidewall surface
Li/Li cell
Sidewall surface (top view)
Li
Separator
Li
Max
200 μm
Min
Photoacoustic imaging